T-tail transonic flutter wind tunnel test part 2 : numerical restitution

Sylvie Dequand, Valentin Lanari

International Forum on Aeroelasticity and Structural Dynamics
IFASD 2024
17-21 June 2024, The Hague, The Netherlands

T-TAIL TRANSONIC FLUTTER WIND TUNNEL TEST PART 2 : NUMERICAL RESTITUION

Sylvie Dequand[1], Valentin Lanari[1]

[1] DAAA, ONERA, Institut Polytechnique de Paris, F-92320 CHATILLON, FRANCE

Keywords: Aeroelasticity, Simulation, High-Fidelity, Pulse, DLM, T-tail, Fluid-structure coupling, Test restitution, Flutter.

Abstract: The article presents the main results of the numerical restitution of the test campaign carried out on a T-tail flutter model in subsonic and up to high transonic domains. The wind tunnel tests were carried out in ONERA's S2MA pressurized wind tunnel at the end of 2022 as part of the Clean Sky 2 airframe ITD program, and will be presented in a companion article [1].

Numerical results obtained with high-fidelity fluid-structure coupling simulations performed with the CFD solver elsA (proprietary ONERA-Safran) [2] are compared with wind tunnel test data and low-fidelity numerical results.

Four T-tail configurations were measured during the test campaign, in order to explore the influence of yaw angle and dihedral on flutter behavior. These different geometries were also used to assess the ability of our numerical tools to predict corner flow aerodynamic phenomena occurring in the region of tail surface intersections.

A good correlation is obtained between numerical and experimental steady pressure coefficients, even at elevated Mach numbers. Regarding unsteady pressure coefficients, aerodynamic responses were computed for a forced motion applied to the T-tail model, and the effects of different excitation parameters were evaluated.

The aeroelastic stability of different T-tail configurations was also studied, and high-fidelity coupled simulations were used to predict the evolution of critical pressure as a function of Mach number.

1 INTRODUCTION

The study of aeroelastic phenomena is an integral part of the advancement of modern aerospace design, particularly in the quest for improved performance and safety. Among the various aerodynamic configurations, T-tails are notable for their susceptibility to flutter, a phenomenon that can lead to catastrophic structural failure if not addressed.

T-tail flutter is caused by the aeroelastic coupling between horizontal and vertical tailplanes, and the aeroelastic stability analysis of such configurations is not obvious because the methods used have been mostly developed for wing flutter and are therefore not specifically suitable for T-

tailplanes. In this context, classical approaches to aeroelastic stability analysis have been adapted and enhanced. Hence, Van Zyl [3] proposes an extension of the Doublets Lattice Method to account for additional aerodynamics loads. The subject of flow interaction between horizontal and vertical parts VTP/HTP interaction has been also investigated using CFD-based aeroelastic simulations ([4], [5]).

The present study focuses on the numerical analysis of T-tail flutter models in subsonic and up to high transonic domains, with three different yaw angles. This study is based on a series of wind tunnel tests carried out in ONERA's S2MA pressurized wind tunnel in late 2022. These tests were carried out as part of the Clean Sky 2 airframe Integrated Technology Demonstrator (ITD) program. The experimental part is presented in a companion paper [1] with details on the flutter model design, and the sealing system solution designed by ONERA to highly reduce the air leakage observed in a previous wind tunnel campaign ([6], [7]).

The first part of this article gives a brief description of the wind-tunnel tests and the different T-tail geometries. Next, the numerical approaches used for the restitution of the different kind of measurements are presented, and in the main results are shown in the last section.

2 WIND-TUNNEL TESTS

2.1 Flutter model

The T-tail transonic flutter wind-tunnel test campaign was carried out in 2022 in ONERA's S2MA transonic pressurized wind tunnel, following an initial test campaign in 2016 ([6], [7]). These wind tunnel tests were funded by the Joint Technology Initiative JTI Clean Sky 2, AIRFRAME Integrated Technology Demonstrator platform "AIRFRAME ITD" (contract N. CS2-GAM-AIR-2020-21-04) being part of the Horizon 2020 research and Innovation framework program of the European Commission.

Figure 2-1: 1/8-scale flutter T-tail model wall mounted in the ONERA's S2MA transonic pressurized wind tunnel.

The 1/8-scale flutter model used in 2016 was redesigned to improve the quality of the new experimental database. Hence, particular attention was paid to the design of a sealing system solution aimed at reducing the air leakage phenomenon that occurred during the first test campaign, at the junction between the fixed fuselage and the T-tail model. Another modification of the first flutter model was the addition of a T-tail junction fairing to decouple the aerodynamic effects between the vertical and horizontal stabilizer and to reduce significantly the corner flow

separation. As for the first flutter model, the new model was designed in such a way that the flutter mechanism is the result of a coupling between two structural modes, which are a roll and a pitch mode of the model.

Contrary to a real aircraft T-tail, the flutter model is rotated by 90° such that the horizontal tailplanes are actually in the vertical direction (Figure 2-1). Therefore, in this article, the vertical T-tailplanes are denoted "VTP" and the horizontal tailplane is denoted "HTP". During the test campaign, different tailplane geometries were studied by varying the dihedral and yaw angles of the vertical section. The results shown in this article focus on the geometries with different yaw angles and 0° dihedral.

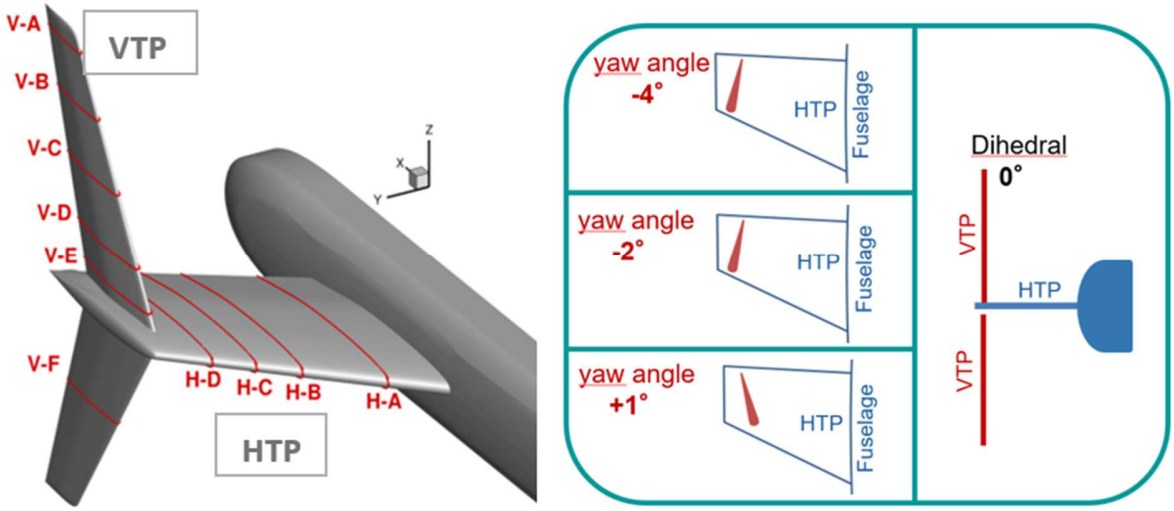

Figure 2-2: [Left] Position and name of the different slices over the HTP and VTPs.
[Right] Configurations "T-2", "T-4" and "T+1" corresponding to three different yaw angles.

Three types of measurements were carried out during the test campaign and are described in details in [1].

For steady pressure measurements, steady aerodynamic data were measured at different slices over the HTP and the two VTPs as shown in Figure 2-2. For unsteady pressure measurements, a pitching motion was applied to the model using a remotely controlled electro-hydraulic system. For these pressure measurements, the effects of angle of incidence, Pi and excitation frequency were studied.

For flutter measurements, the critical pressure was determined by continuously increasing the stagnation pressure. A safety actuator was used to quickly stop the flutter phenomenon before any failure of the setup occurred.

3 NUMERICAL APPROACH

High-fidelity simulations are performed with the elsA CFD code (ONERA-Airbus-Safran property) [2], using its aeroelastic module "elsA-Ael". The aeroelastic computations are based on a modal approach for the structure. The URANS computations are performed with a centered finite-volume discretization on a structured mesh, a backward-Euler scheme with implicit LUSSOR relaxation for the time integration, and a 2nd order central Jameson scheme for the spatial discretization. All the URANS computations have been performed with the Spalart-Allmaras turbulence model, for Mach numbers from 0.7 up to 0.925.

3.1 Aerodynamic meshes

An aerodynamic mesh was built around the “T-2” T-tail geometry. The mesh is a structured mesh of about 19 millions cells (Figure 3-1). The walls of the wind tunnel were not modelized and only the wall on which the model was mounted was taken into account by applying a wall boundary condition on the grey boundary shown in Figure 3-1. All the other far-field mesh boundaries were set to non-reflective boundary conditions.

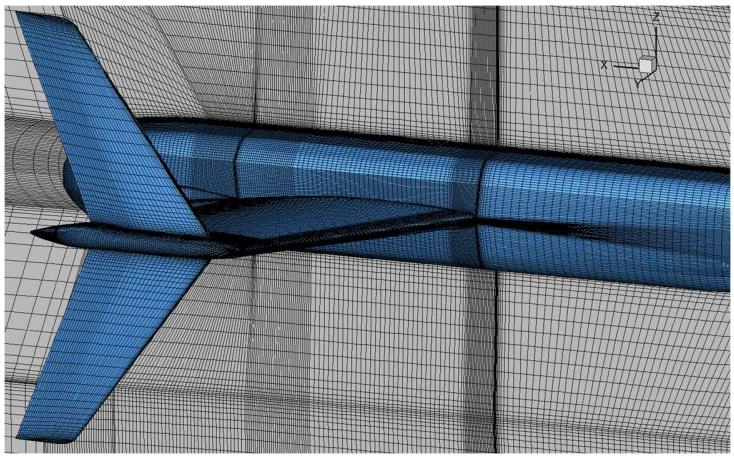

Figure 3-1: Aerodynamic structured mesh around the “T-2” T-tail flutter model.

For the other T-tail configurations, the structured aerodynamic meshes have been generated by mesh deformation techniques included in a modular library currently developed at ONERA for aeroelastic calculations and using the IDW method (Inverse Distance Weighting). For our particular need here, the mesh deformation module has enabled to generate very efficiently the new aerodynamic meshes from the initial mesh already built (Figure 3-2).

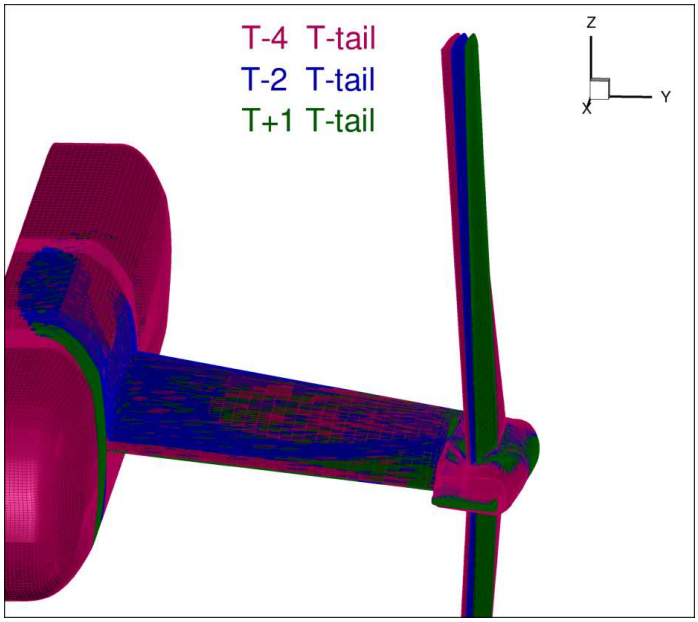

Figure 3-2: Visualization of the skin around the “T-4”, “T-2” and “T+1” T-tail geometries.

3.2 Steady and unsteady pressure computations

For the steady and unsteady measurements, the shaft of the T-tail flutter model is connected to the hydraulic actuator which controls the angle of incidence of the model. In this "pressure configuration", the roll and pitch degrees of freedom are blocked.

The numerical restitution of the steady pressure measurements was performed by rigid RANS computations using our high-fidelity CFD code elsA (ONERA-Airbus-Safran property) [2].

For the unsteady pressure measurements, fluid-structure coupling simulations were performed using the aeroelastic module "elsA-Ael". These aeroelastic computations are based on a modal approach to define the forced motion applied to the structure.

3.3 Flutter analysis

3.3.1 Modal basis

For the flutter measurements, the stiffness of the roll and pitch degrees of freedom is controlled by a torsion blade and S-beams [1]. Under certain aerodynamic conditions, the coupling of these two structural modes can result in a flutter phenomenon.

An experimental modal analysis of the structural model allows to determine the five first structural modes of the model [1]. The results of this modal analysis are then used by Dassault Aviation to tune their Finite Element Model. The modal basis issued from this Finite Element Model consists in 15 modes (modal shapes, modal frequencies, modal masses). The flutter simulations presented in this paper have been performed using the five first modes of DaV modal basis enhanced with the experimental modal damping values. The modal values are given in the table below. The modal frequencies of the FEM are very close to the experimental modal frequencies. The modal shapes of the two first modes are shown in Figure 3-3. They correspond to the two modes which contribute to the flutter behavior of the system. The first mode corresponds to the roll movement of the model, and the second mode corresponds to the pitch of the model.

Modal basis					
	Mode 1	**Mode 2**	**Mode 3**	**Mode 4**	**Mode 5**
Modal frequency (Hz)	12.36	15.13	29.43	33.37	37.59
Modal mass (kg)	10.16	12.89	6.82	4.91	6.44
Modal damping (%)	0.43	0.81	0.92	1.11	0.92

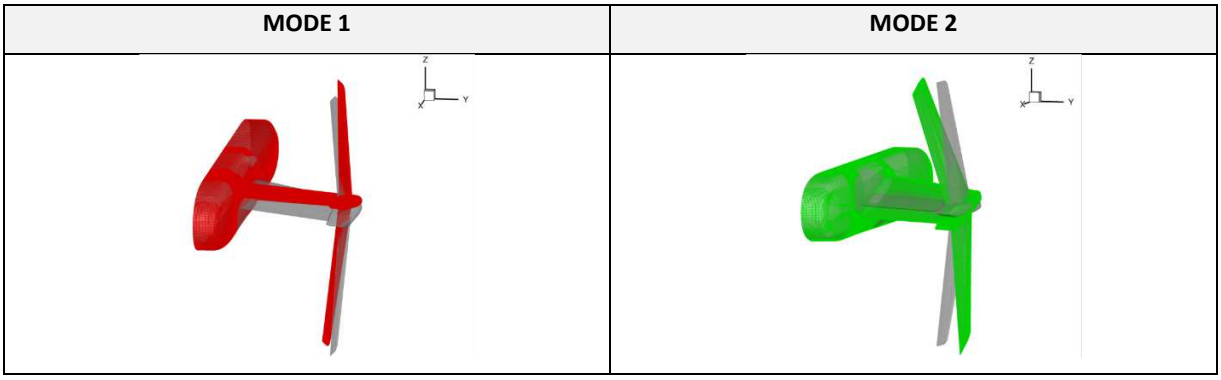

Figure 3-3: Modal deformations of mode1 (left) and mode 2 (right) on the skin of the T-2 T-tail CFD mesh. The grey surfaces represent the initial undeformed mesh.

3.3.2 High-fidelity method

3.3.2.1 Pulse method

The numerical restitution of the flutter measurements was mainly performed using the "Pulse" method implemented into the aeroelastic module "elsA-Ael" of the CFD code elsA [11].

In this method, the structural model is excited by a forced motion corresponding to a Heaviside function (step function from 0 to 1, at a given initial instant). The forced motion is applied to each structural mode one by one and the impulse response of the structure is computed in a single simulation for a full frequency range.

The Generalized Aerodynamic Forces (GAF) of the system can be written as a function of a transitory part $T(i,t)$ (unsteady response of the system without excitation) and the impulse response $h(i,j,t)$:

$$GAF(i,j,n\Delta t) = T(i,n\Delta t) + e_0 \Delta t \sum_{k=0}^{n} h(i,j,k\Delta t) \tag{1}$$

where Δt is the time step, $n\Delta t$ is the current time, and e_0 is an amplification factor.

The GAF can then be determined by means of a classical Fourier analysis of the time responses:

$$\hat{f}(\omega) \approx \Delta t \sum_{k=0}^{n} f(k\Delta t) e^{-i\omega k\Delta t} \tag{2}$$

The computation of the GAF in the frequency domain allows to solve the aeroelastic stability problem (1) using the classical double scanning "p-k" method ([8], [9]).

$$\left[p^2\mathbf{M} + p\mathbf{C} + \mathbf{K} - q_{dyn}\mathbf{GAF}(M,k)\right]\mathrm{X}(p) = 0 \tag{3}$$

where **M**, **K**, **C** are respectively the modal mass, stiffness and damping matrices, q_{dyn} is the freestream dynamic pressure, X is the modal coordinate vector, *M* is the Mach number and *k* is the reduced frequency.

3.3.2.2 Direct Coupling method

The numerical results obtained with the Pulse method described in the previous section have been compared with numerical results obtained with the so-called 'Direct Coupling' method. This

method is described in details in [12]. In this approach, several dynamic fluid-structure coupling simulations are performed at different stagnation pressures, with an initial modal velocity applied to each structural mode. The time response of the system enables to determine the critical stagnation pressure at which the system becomes unstable. However, the method requires several computations and can be very time consuming. Therefore, only a few results obtained with this method are shown in this paper.

3.3.3 Low-fidelity method

The Generalized Aerodynamic Forces (GAF) can also be computed using the Doublet Lattice Method (DLM) [10]. This linear method in frequency domain is valid in the subsonic domain and, in addition to the experimental database, provides an efficient tool for comparison with our high-fidelity numerical methods, at least for low Mach numbers.

The aerodynamic mesh used in the DLM is shown in Figure 3-4, with a visualization of the two first mode shapes. It consists of five panels representing each surface of the flutter model (fuselage, HTP, fairing, and the two VTPs). This method does not take into account the yaw angle of the different T-tail geometries.

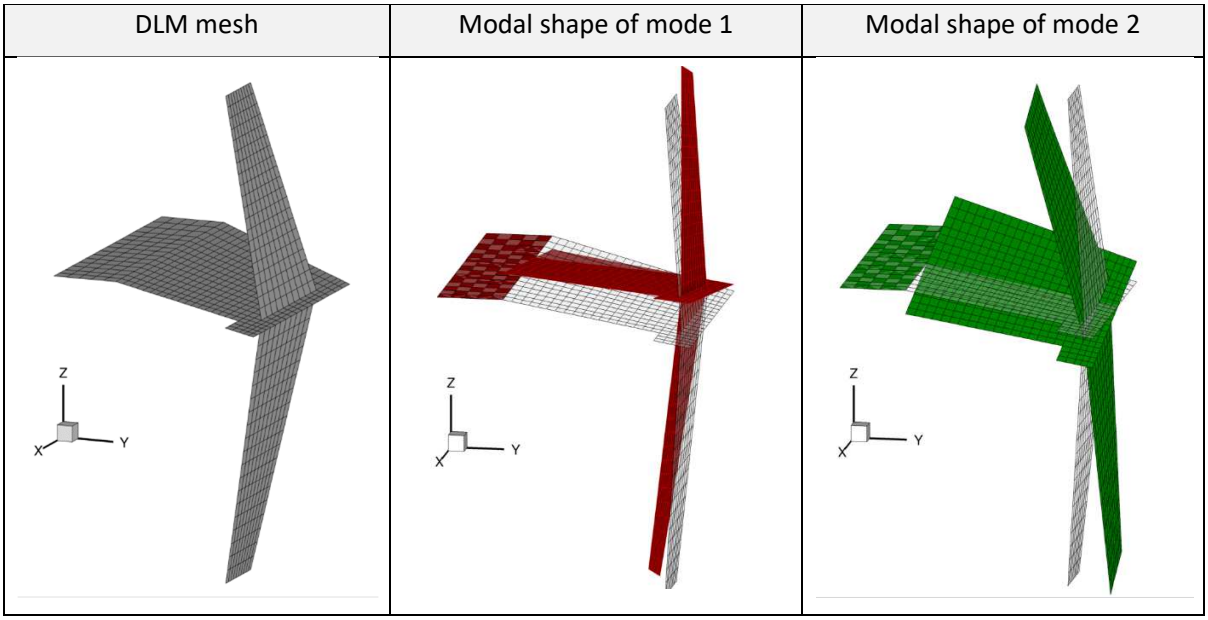

Figure 3-4: Aerodynamic DLM mesh (left), modal deformations of mode 1 (center) and mode 2 (right). The grey surfaces represent the undeformed DLM mesh.

3.3.4 Smoothing method

In Figure 3-4, the modal deformations of modes 1 and 2 clearly show that the fuselage part of the flutter model remains immobile (as in the experimental setup, where a gap of 5mm exists at the fuselage/HTP junction). This discontinuity between the fuselage immobility and the movement of the HTP is not a problem with DLM. However, in our high-fidelity simulations, the aerodynamic structural mesh must remain continuous even in the presence of large deformations.

A particular treatment is further performed at the junction between the HTP and the fuselage of the model, in order to avoid the apparition of negative volume cells in the structured aerodynamic mesh. The technique consists in selecting a local zone on the fuselage around the junction with the

HTP, on which small deformations will be allowed. The smoothing of this local zone can be adjusted by tuning coefficients acting on the deformations in the different directions. The modal deformations resulting from this smoothing technique at the HTP/fuselage junction are shown in Figure 3-5 for mode 1 and 2, with a factor of 20 for a better visualization.

This smoothing technique is very efficient in the case of classical configurations such as a wing attached to a fuselage. However, in the particular case of T-tail geometries studied here, a small change in the local deformation of the HTP could affect the deformation of the VTPs.

Therefore, the aerodynamic mesh used for high-fidelity simulations has further been modified to better represent the experimental flutter model. As in the experimental setup, a gap of 5 mm has been added between the fuselage and the HTP, to allow the free deformation of the HTP. The new mesh deformation due to the two first modes are shown in Figure 3-6.

In Figure 3-7 and Figure 3-8, the modal shapes with and without the gap are plotted for each slice over the HTP (Figure 3-7) and the VTPs (Figure 3-8) as described in Figure 2-2. Only very small changes (around 1% for H-A and H-C slices, and around 2% for H-B slice) can be seen on the slices near the fuselage/HTP junction. The presence of the gap does not affect the modal shapes of the VTP.

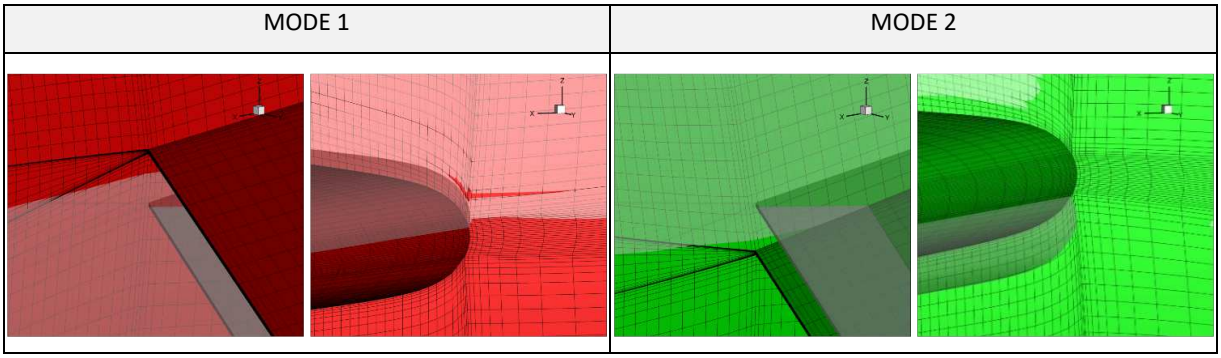

Figure 3-5: Modal deformations of modes 1 and 2 at the HTP/fuselage junction. The grey surfaces in translucency represent the non-deformed mesh.

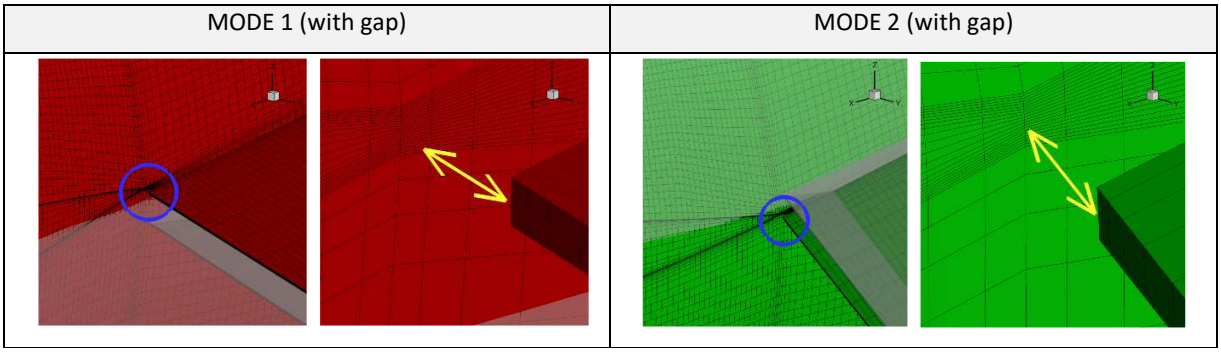

Figure 3-6: Modal deformations of modes 1 and 2 when adding a gap between the fuselage and the HTP. The grey surfaces in translucency show the non-deformed mesh. The yellow arrow represents the gap in the zoomed region of the blue circle.

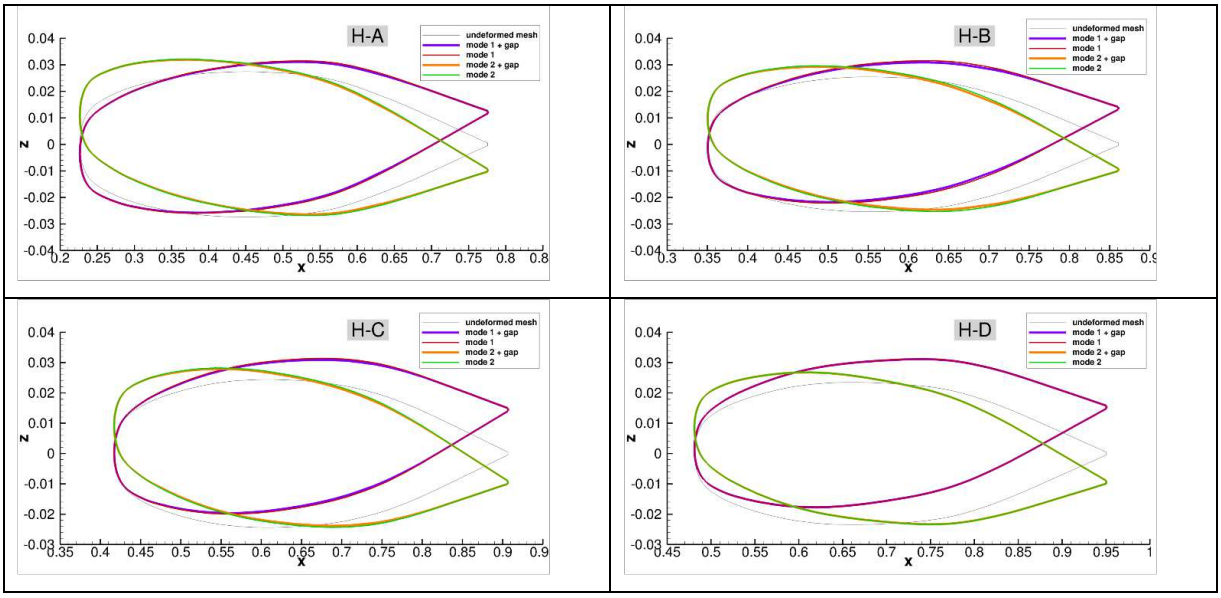

Figure 3-7: Modal shapes with and without the gap between the fuselage and the HTP, at the different slices over the HTP.

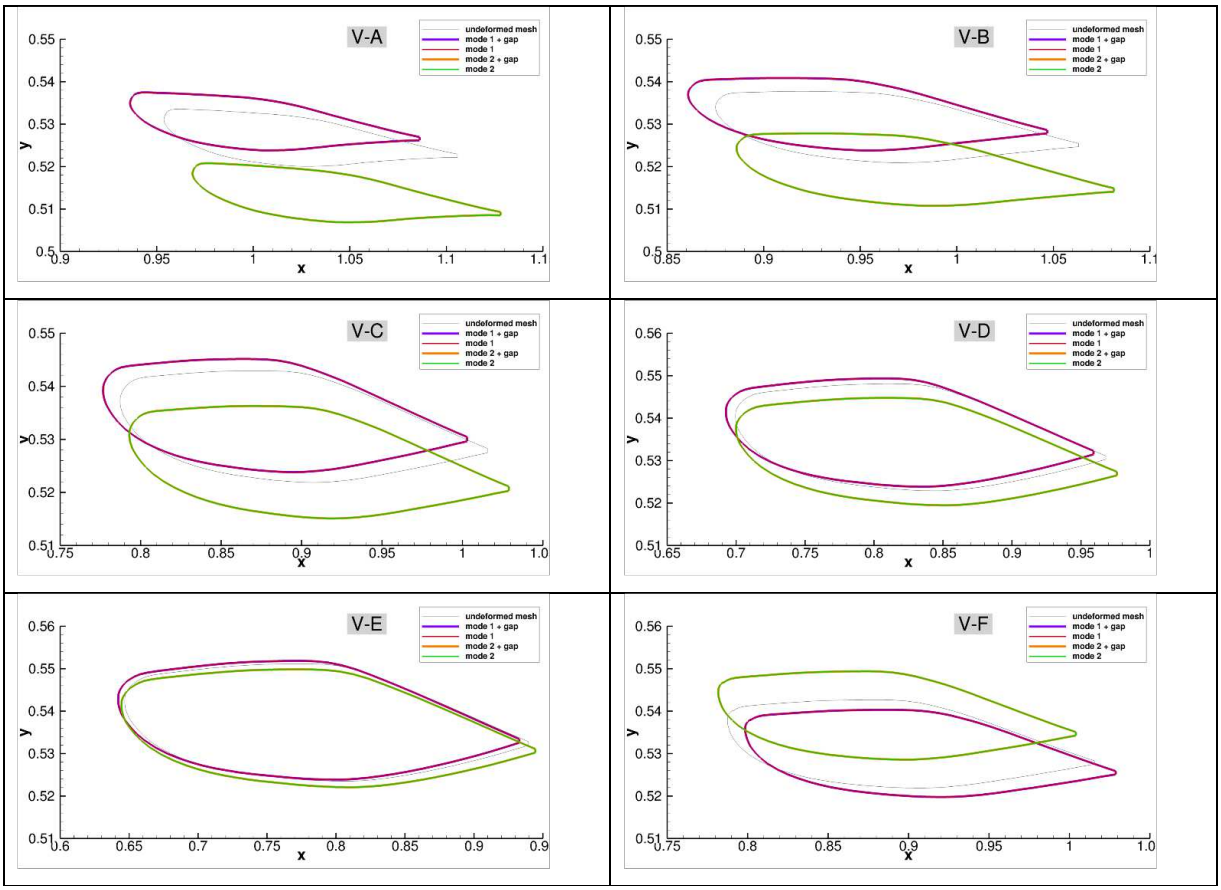

Figure 3-8: Modal shapes with and without the gap between the fuselage and the HTP, at the different slices over the VTP.

4 RESULTS

4.1 Steady pressure coefficients

The numerical steady pressure coefficients are determined by rigid RANS computations without taking into account the structural flexibility. They are given at different slices over the horizontal and vertical tail planes (HTP and VTPs) as shown in Figure 2-2.

4.1.1 Effect of Mach number

Figure 4-1 shows numerical steady pressure coefficients obtained with the T-2 T-tail configuration at three different Mach numbers (Mach = 0.7, 0.85 and 0.925). For the sake of readability, experimental data are given only for Mach number 0.85.
The slices H-C and V-C shown on Figure 2-2 are located near the middle of the HTP and VTPs, and the slices H-D and V-E are located close the HTP/VTP junction. On the HTP surface, increasing the Mach number results in the apparition of a second shock around 20% of chord, while the first shock (around 60% of chord) increases. On VTP "inner" surfaces (on the fuselage side), the increase in Mach number (from 0.7 to 0.85) increases the second shock (at 50% of chord).

The complete analysis of the experimental and numerical steady data for the different aerodynamic conditions (Mach number, pressure, angle of incidence…) has shown a very good correlation between the numerical and experimental steady pressure coefficients, even at higher Mach numbers.

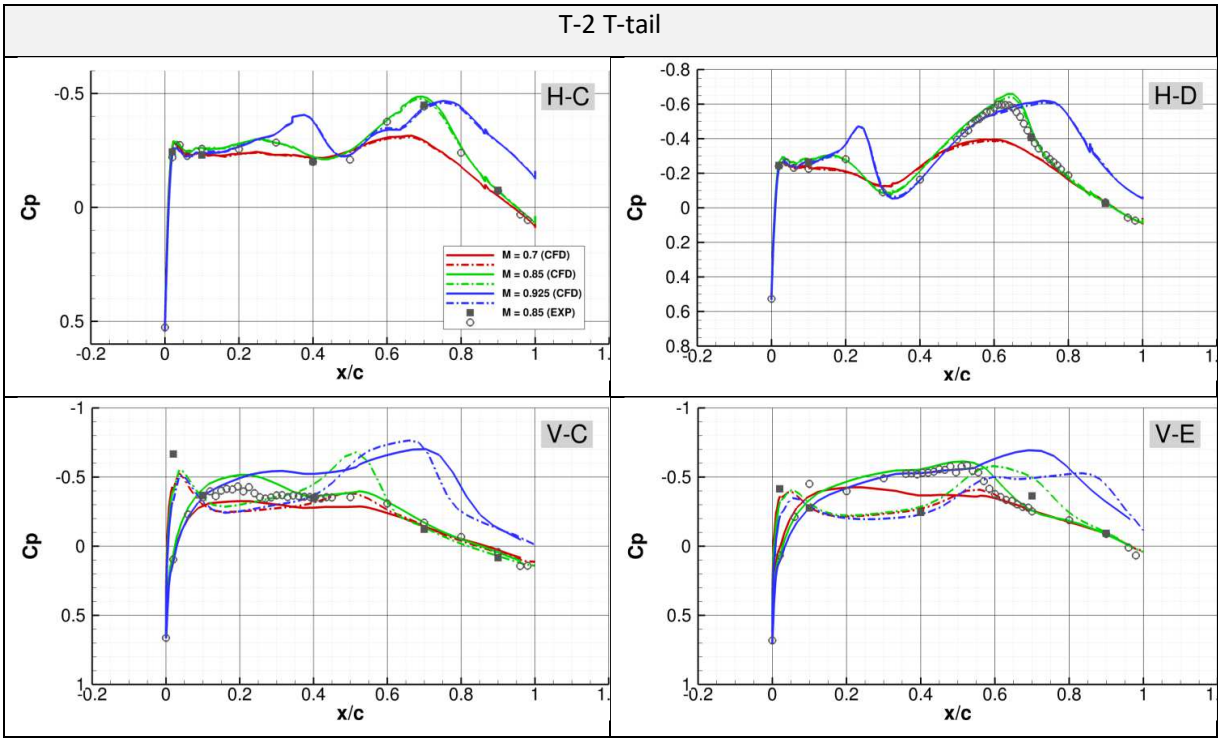

Figure 4-1: T-2 T-tail - Mach effect on steady pressure coefficients at two slices over the HTP (upper graphs) and VTP (lower graphs) surfaces.

4.1.2 Effect of yaw angle

Figure 4-2 presents the numerical steady pressure coefficients obtained at Mach number 0.7 for three different yaw angles (-4°, -2° and +1°). Experimental data are only shown for the reference empennage configuration (T-2).

On the HTP surface, the passage from a yaw angle of -4° to +1° results in a decrease of the pressure with a more important shock, due to the confinement of the flow. On the VTP surfaces, the change from a negative to a positive yaw angle induces a change of behavior of the pressure coefficient between inner and outer VTP surfaces, and the absolute value of the outer pressure becomes higher than that of the inner pressure.

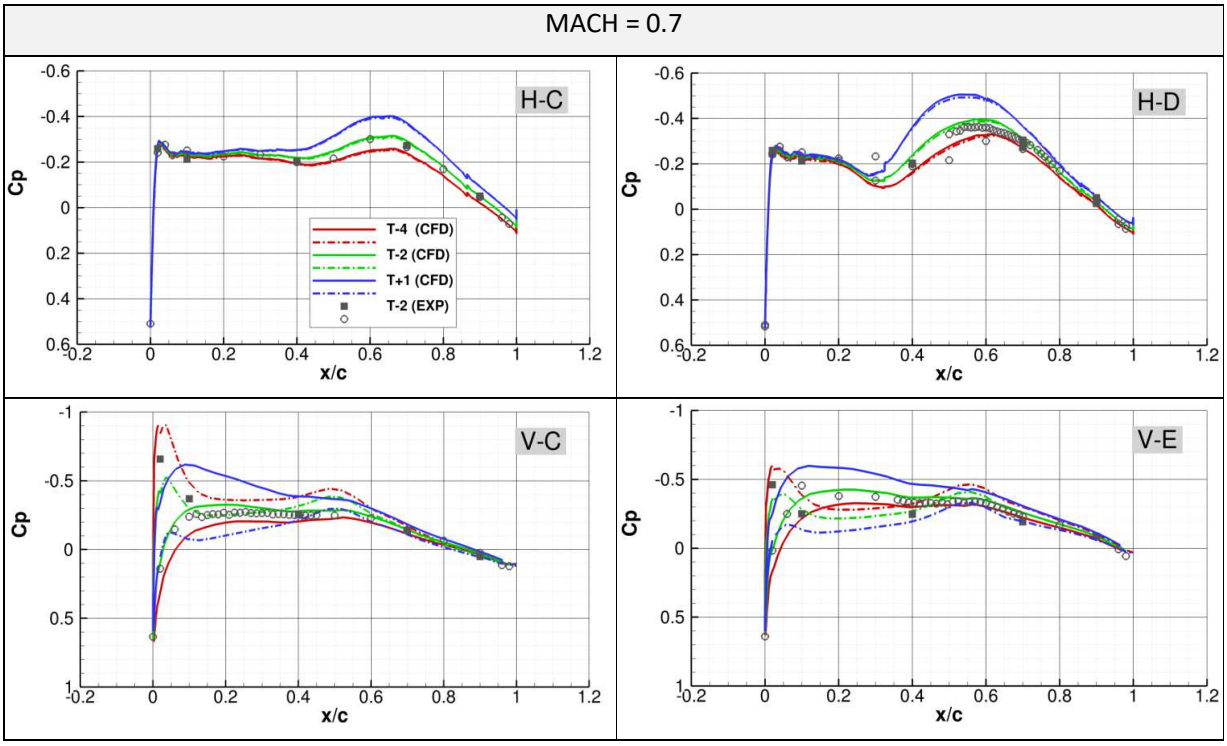

Figure 4-2: Mach = 0.7 – Yaw angle effect on steady pressure coefficients at two slices over the HTP (upper graphs) and VTP (lower graphs) surfaces.

For comparison, the same graphs are plotted in Figure 4-3 for Mach number 0.925 for the three different yaw angles. Again, experimental data are only shown for the T-2 T-tail.

Globally, on the VTP surfaces, the same behavior as at Mach number 0.7 is observed at Mach number 0.925, between the steady pressure coefficients of the negative and positive yaw angles.

At Mach number 0.925, a second shock appears around the quarter chord of the HTP. Although the correlation between numerical and experimental data is less good than that at Mach number 0.7, it is still quite good and the evolution of the steady pressure coefficients is well predicted.

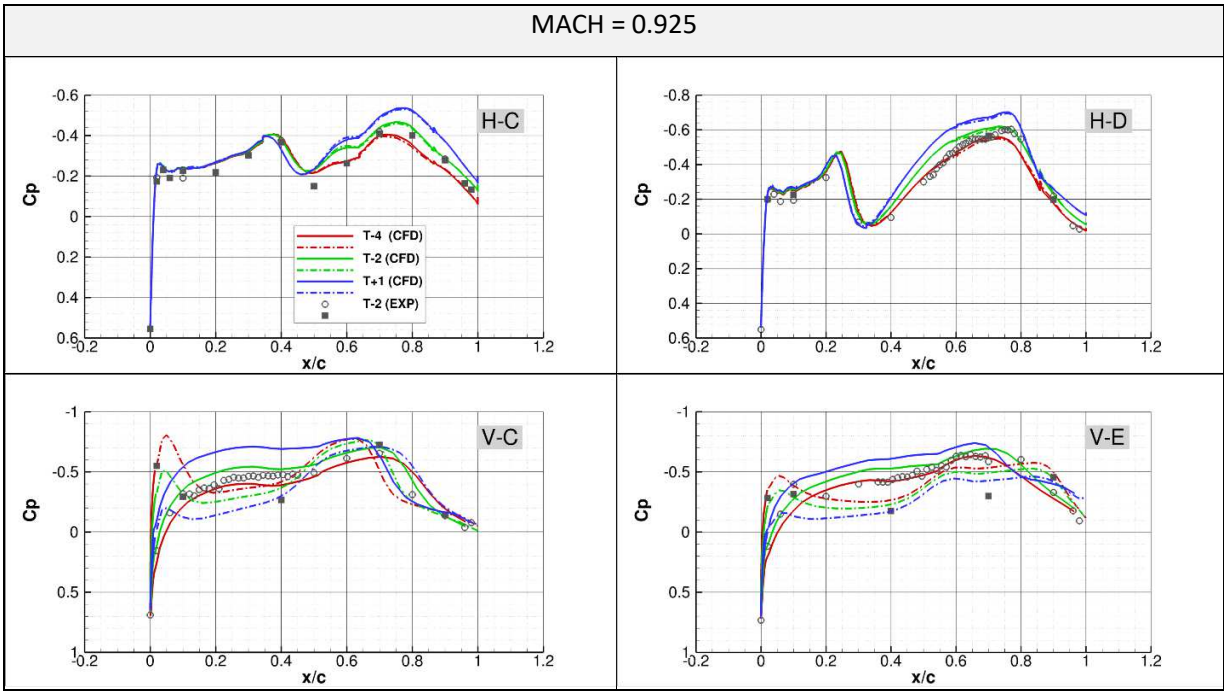

Figure 4-3: Mach = 0.925 – Yaw angle effect on steady pressure coefficients at two slices over the HTP (upper graphs) and VTP (lower graphs) surfaces.

4.1.3 Gap effect

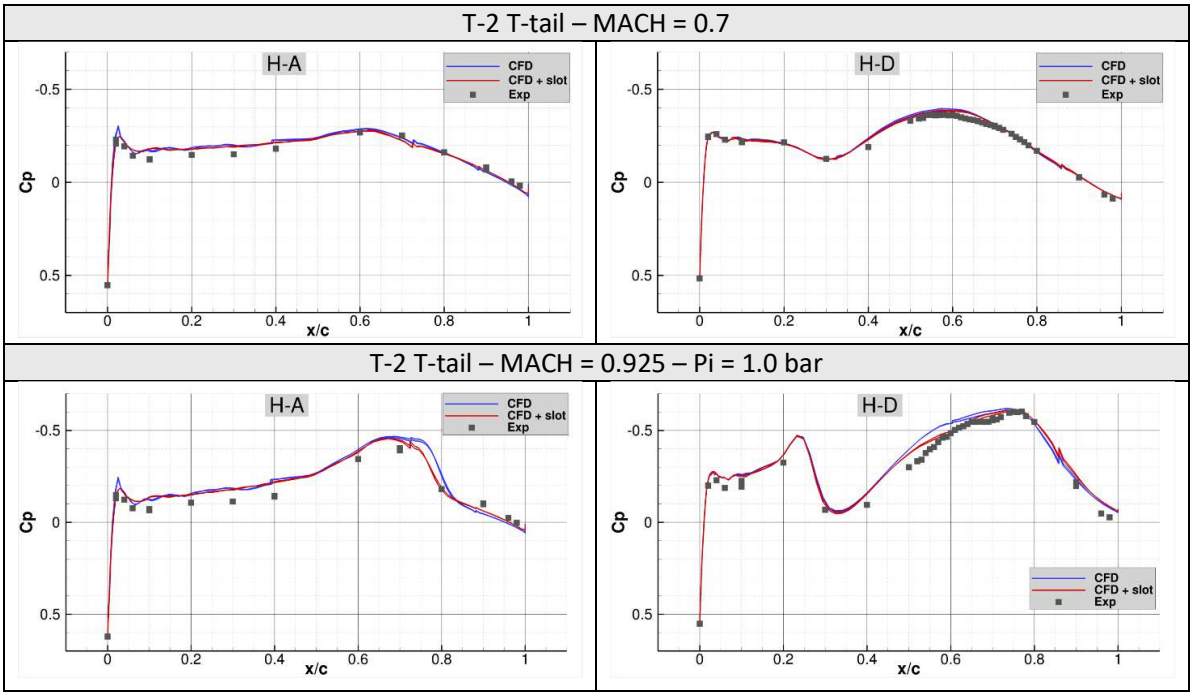

Figure 4-4: T-2 T-tail – Gap effect on steady pressure coefficients at low and high Mach numbers at two slices over the HTP surface.

In Figure 4-4Figure 3-6, numerical steady pressure coefficients with and without the gap between the fuselage and HTP surfaces are compared to experimental data. For low Mach number, the gap effect is quite small and only a small change in the pressure amplitude can be seen at the leading edge for the slice H-A located very close to the HTP/fuselage junction. For higher Mach number, this gap effect can again be seen for the H-A slice, and a second effect is detected. The presence of the gap seems to improve the prediction of the second shock.

4.2 Unsteady pressure coefficients

As for steady coefficients, numerical unsteady pressure coefficients are determined by rigid URANS computations without taking into account the structural flexibility. The excitation pitch motion imposed during wind-tunnel tests is simulated as a harmonic forced motion imposed to the HTP of the model, using the aeroelastic module "elsA-Ael" of the elsA CFD code. The results are given at different slices of the HTP and VTPs as shown in Figure 2-2.

4.2.1 Effect of Mach number

Figure 4-5shows a comparison of the unsteady pressure coefficients obtained for the T-2 T-tail configuration at three different Mach numbers (0.7, 0.85 and 0.925). For the sake of readability, only the experimental data measured at Mach number 0.85 are plotted in the graphs. However, it has been verified that the experimental unsteady pressure coefficients are quite well predicted by numerical simulations at both Mach numbers 0.7 and 0.925.

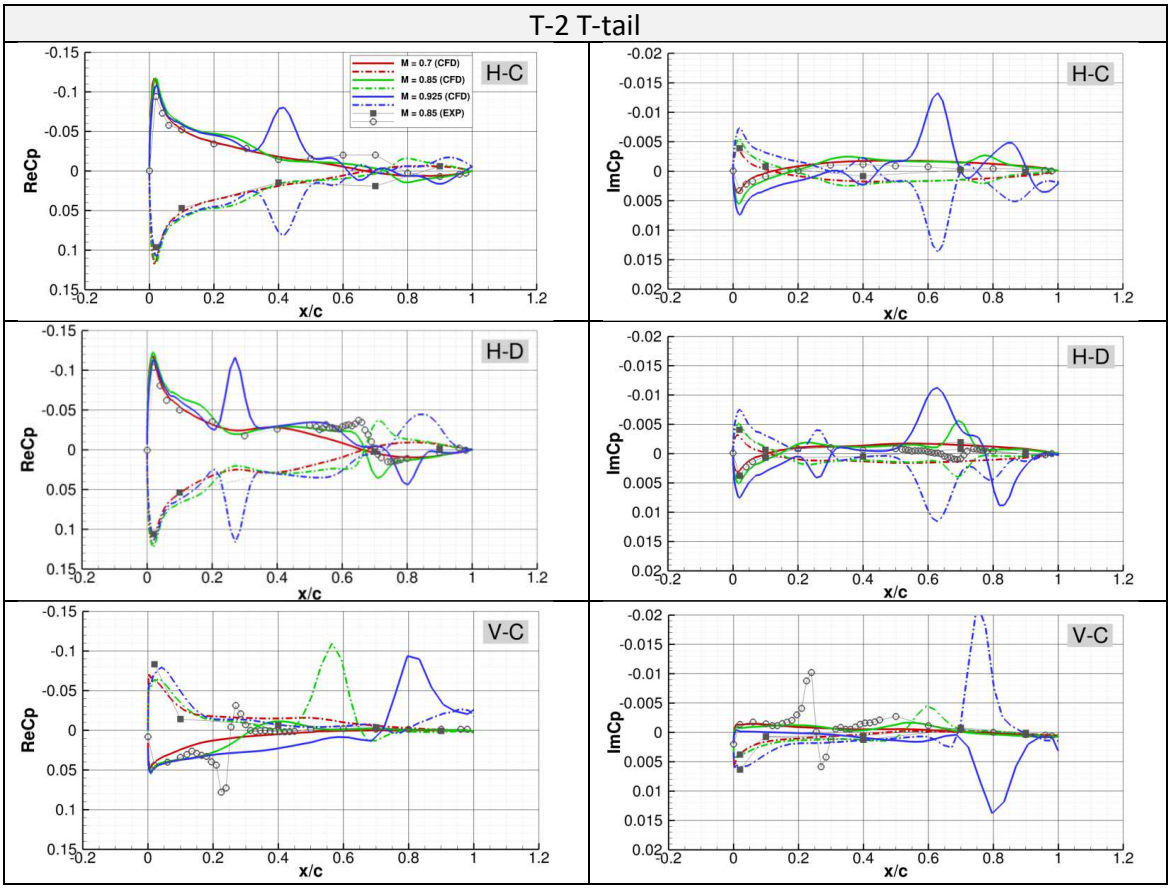

Figure 4-5: T-2 T-tail - Mach effect on unsteady pressure coefficients at slices over the HTP (upper graphs) and VTP (lower graphs) surfaces, with an excitation motion of 5Hz and +/-0.2°.

At Mach number 0.85, the unsteady pressure coefficients are more disturbed and several shocks appear on both the HTP and VTP surfaces. In the vicinity of the HTP/VTP junction (H-D slice), the shocks on the lower walls are predicted quite well in amplitude for the real part, but with a small shift. The imaginary part (ten to twenty times smaller than the real part) is more difficult to predict, particularly at higher Mach numbers (0.85 and 0.925).

At the center of the VTP surface (V-C slice), the shock in the experimental unsteady pressure coefficient at Mach 0.85 is not predicted at all by the numerical simulations. This shock appears also at Mach 0.925 but at the V-E slice (close to the T-tail fairing).

4.2.2 Effect of yaw angle

In Figure 4-6 and Figure 4-7, the real and imaginary parts of the unsteady pressure coefficients are plotted for three different yaw angles (-4°, -2° and +1°), respectively at Mach numbers 0.7 and 0.925. Experimental data are given only for the T-2 T-tail, for better readability.

At Mach number 0.7 (Figure 4-6), the yaw angle has a very small effect on the unsteady pressure coefficients, compared to its effect on the steady coefficients.

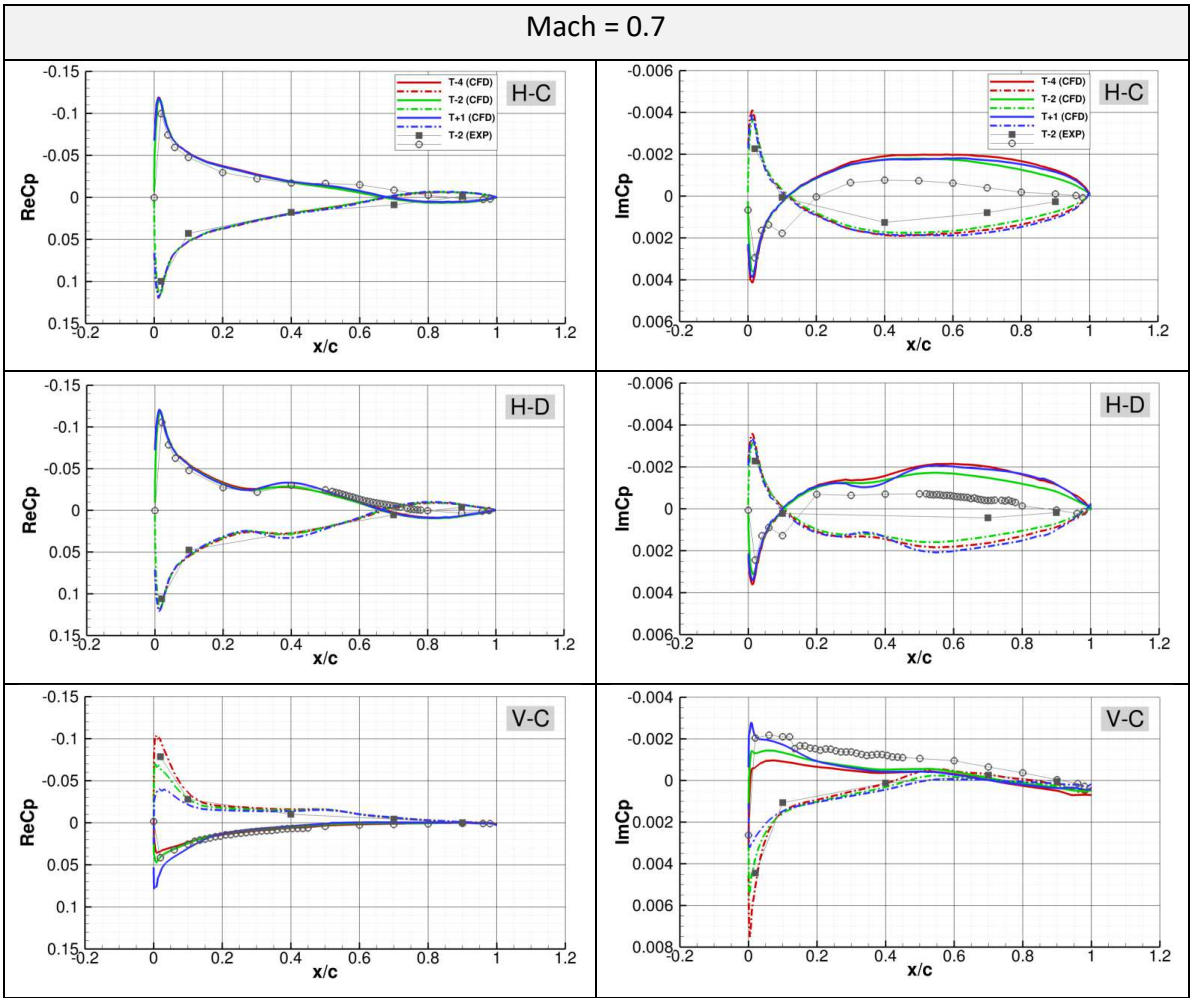

Figure 4-6: Effect of the yaw angle on the predicted unsteady pressure coefficients at Mach number 0.7, with an excitation motion of 5Hz and +/-0.2°.

At Mach number 0.925 (Figure 4-7), the unsteady pressure coefficients are more perturbated and a lot of oscillations appear both for their real and imaginary parts. Again, the numerical restitution of the imaginary part of the unsteady pressure coefficients is more difficult than that of the real part.

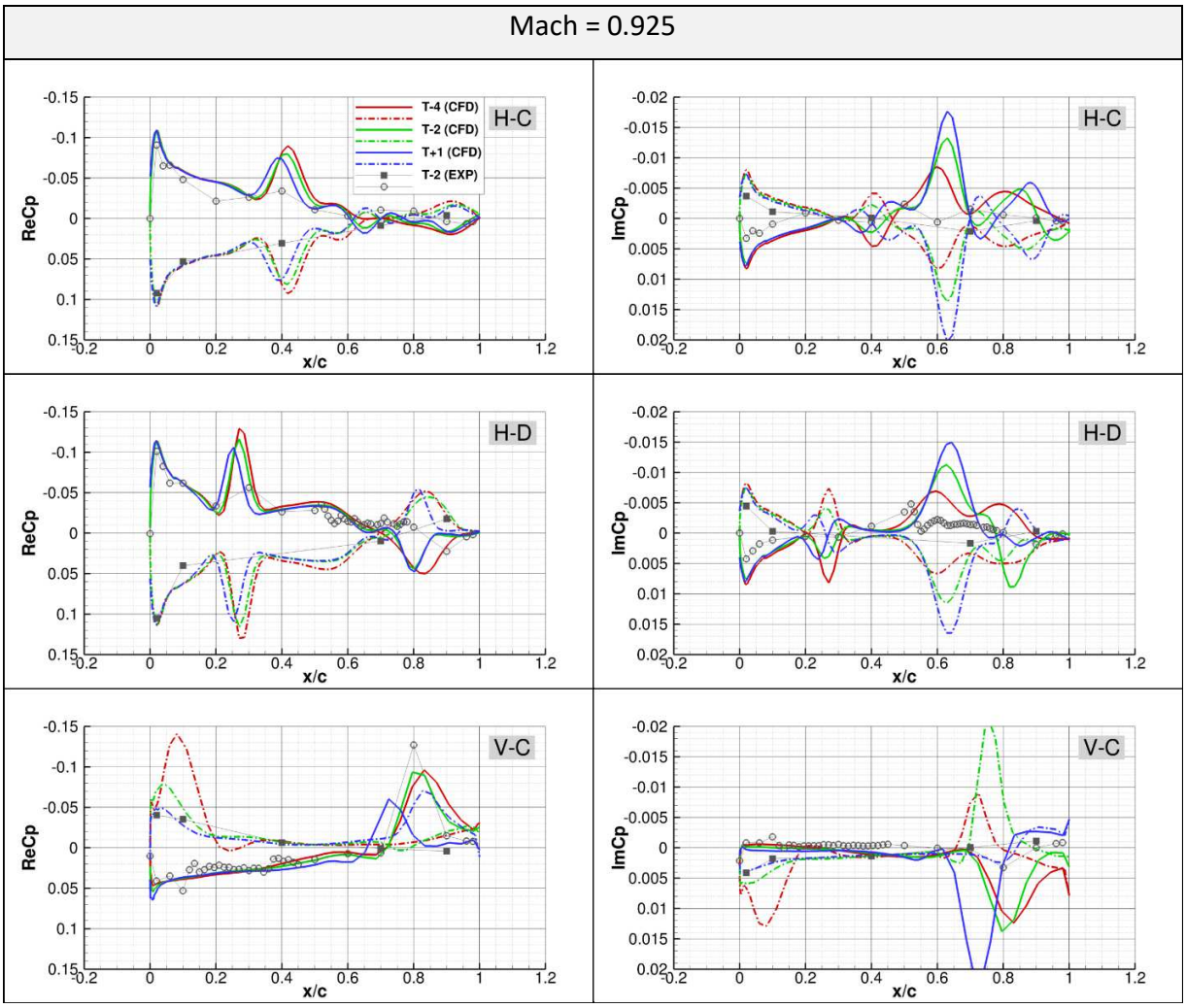

Figure 4-7: Effect of the yaw angle on the predicted unsteady pressure coefficients at Mach number 0.925, with an excitation motion of 5Hz and +/-0.2°.

4.2.3 Effect of the excitation frequency

Figure 4-8 and Figure 4-9 show a comparison between the predicted unsteady pressure coefficients obtained for three different frequencies (5Hz, 15Hz and 30Hz) of the excitation signal applied to the HTP at respectively, Mach number 0.7 and 0.925. Experimental data are given only for the excitation signal of 15 Hz, for better readability.

For low Mach number (Figure 4-8), the real part of the unsteady coefficients is not affected by the excitation frequency. The weak effect of frequency is only visible on the imaginary parts, due to

their very small amplitudes compared to the real parts. In general, increasing the frequency results in an amplification of the imaginary part, without changing its behavior.

For higher Mach number (Figure 4-9), the effect of the excitation frequency is more visible. The real part of the 5Hz and 15Hz excitation signals is quite similar, but the simulation with a 30Hz excitation signal shows a small decrease in the real part of the unsteady pressure coefficients. The imaginary parts of the unsteady pressure coefficients show a lot of oscillations. Although the amplitude is underestimated, the global evolution of the unsteady pressure coefficients is rather quite well caught by the simulations.

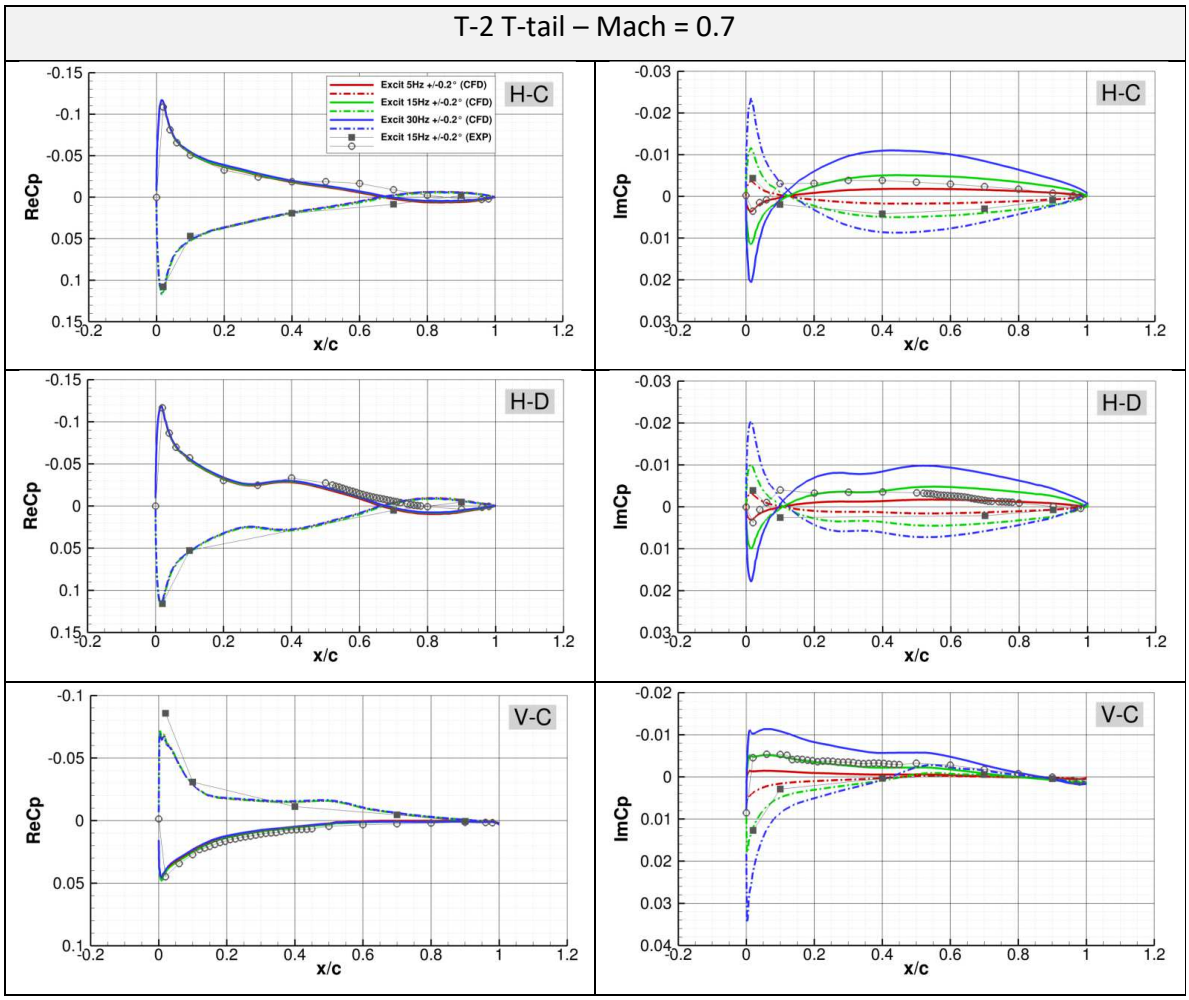

Figure 4-8: T-2 T-tail - Effect of the excitation frequency on the predicted unsteady pressure coefficients at Mach number 0.7.

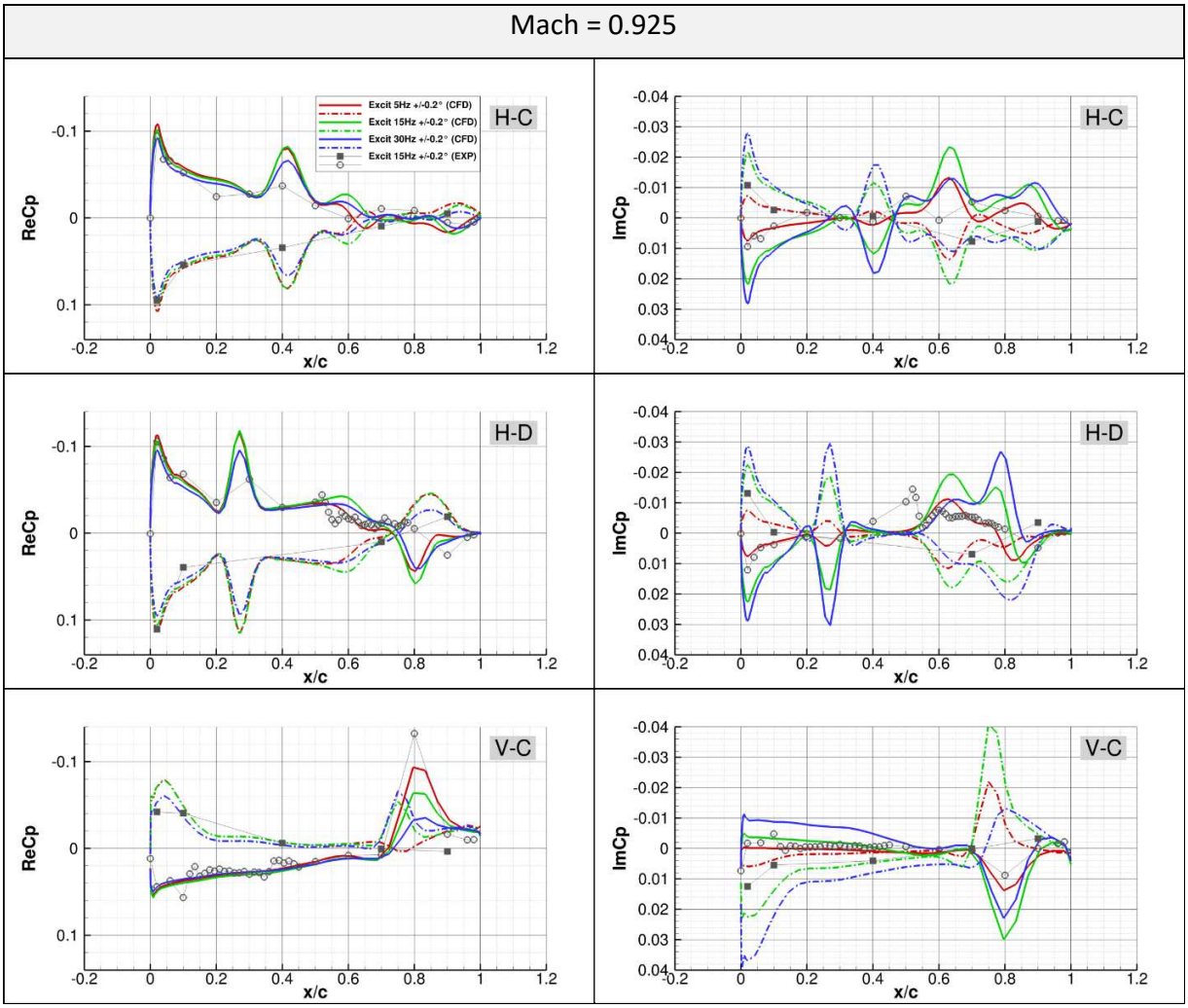

Figure 4-9: T-2 T-tail - Effect of the excitation frequency on the predicted unsteady pressure coefficients at Mach number 0.925.

4.2.4 Gap effect

Figure 4-10 and Figure 4-11 show a comparison of the numerical unsteady pressure coefficients with and without the gap at the interface between the fuselage and the HTP surfaces, for different slices over the HTP and VTP surfaces, respectively at Mach numbers 0.7 and 0.925.

At Mach 0.7 (Figure 4-10), for the real part of the unsteady pressure coefficients, the presence of the gap radically improves the predicted real part of the unsteady pressure coefficients. In particular, the unexplained pressure intersection around 60% of the chord disappears in the presence of the gap.

However, at Mach number 0.925 (Figure 4-11), the presence of the gap does not particularly improve the predicted pressure coefficients.

In the same way, for what concerns the imaginary part of the unsteady pressure coefficients, the predictions are not improved by the presence of the gap.

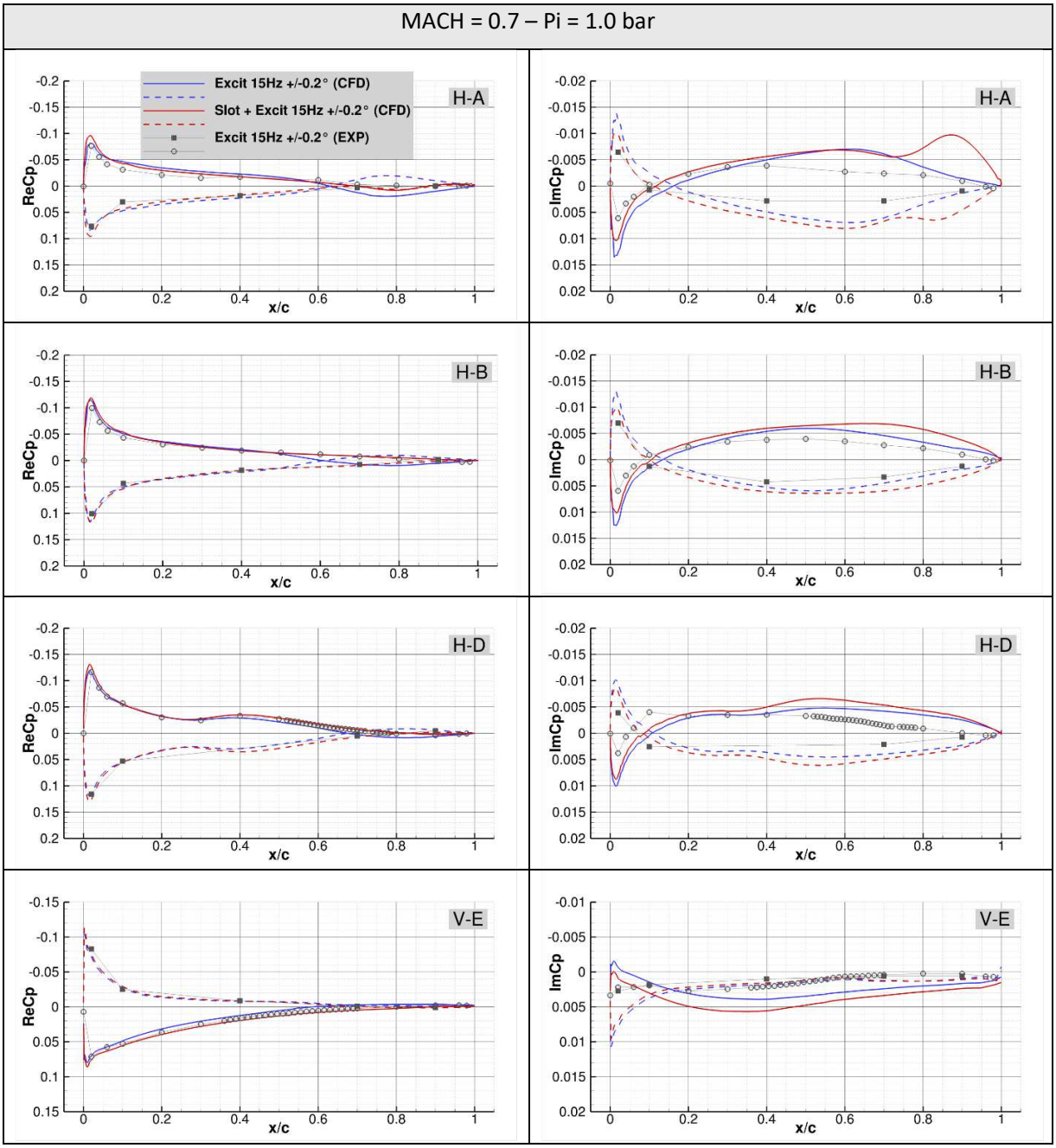

Figure 4-10: T-2 T-tail – Gap effect on unsteady pressure coefficients at Mach number of 0.7 at different slices over the HTP and VTP surfaces.

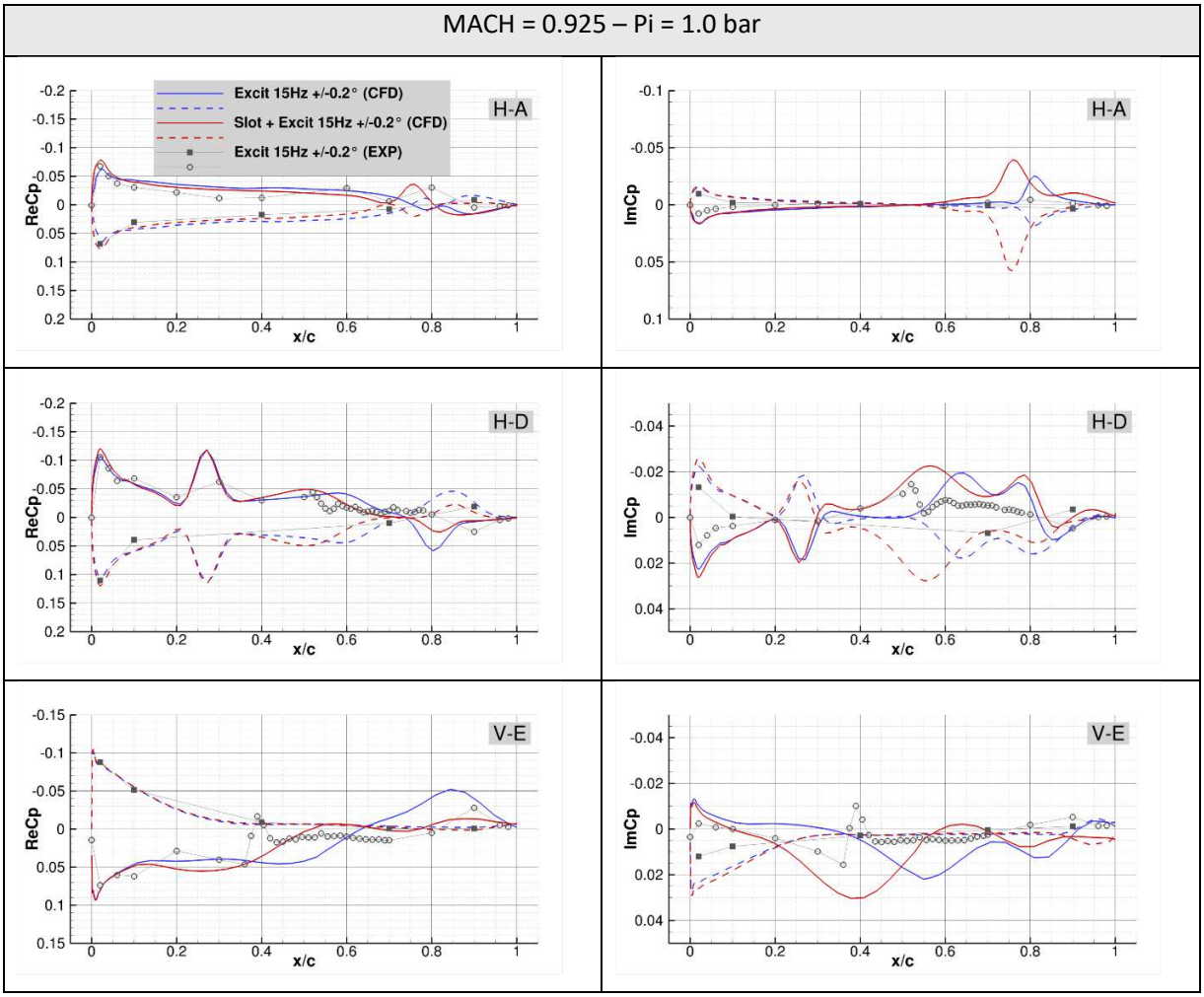

Figure 4-11: T-2 T-tail – Gap effect on the predicted unsteady pressure coefficients at Mach number 0.925 at different slices over the HTP and VTP surfaces.

4.3 Flutter analysis

As described in section 3.3.2, the pulse method enables to compute the GAF of the system, and the flutter analysis is then performed in a post-processing step by using a classical p-k method. This flutter analysis allows to determine the critical stagnation pressure, at which the flutter phenomenon appears.

Figure 4-12 shows the evolution of the critical stagnation pressure with the Mach number for the three T-tail geometries T+1, T-2 and T-4. In the three graphs, the plotted red line corresponds to the results obtained with the Pulse method and the plotted grey line corresponds to the experimental data. For the three T-tail geometries, the critical stagnation pressure is underestimated by around 0.3 bar. At the center of Figure 4-12, corresponding to the T-2 T-tail,

the single points added into the graph correspond to the results obtained with the Direct Coupling method. Both numerical methods (Pulse and Direct methods) are therefore predicting equivalent critical stagnation pressures for different Mach numbers. The green dashed line corresponds to the DLM results. The critical stagnation pressure seems better predicted by DLM than by the Pulse method, even for high Mach numbers, when the method is no longer valid

At higher Mach numbers, it is interesting to see that the Pulse method is able to predict the Mach number effect on the critical pressure. This nonlinear "bump" behavior is less visible for the positive yaw angle (T+1 configuration) but a kind of stagnation in the critical pressure value can nevertheless be observed between Mach numbers 0.85 and 0.9. For the T-4 configuration, the Mach number effect is not visible on the experimental data but probably delayed at higher Mach The numerical simulations predict a kind of inverted bump at higher Mach numbers, between Mach numbers 0.85 and 0.925.

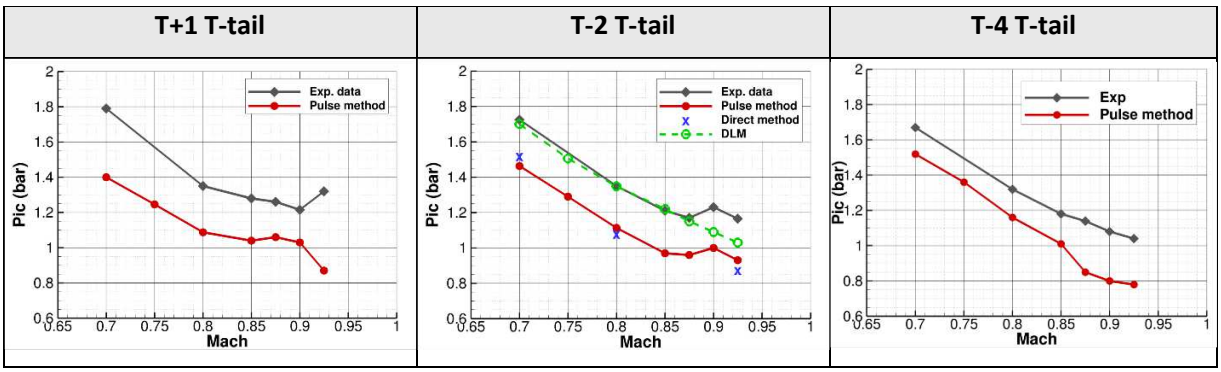

Figure 4-12: Evolution of the critical stagnation pressure with Mach number for the configurations T+1 (left-hand side), T-2 (center) and T-4 (right-hand side).

Figure 4-13 shows the same results than in Figure 4-12 but the data are all superposed in order to check if our numerical model is able to predict the yaw angle effect between the three T-tail geometries.

At lower Mach numbers up to 0.82, the numerical simulations are predicting the inverse behavior than that expected and experimentally measured. The red dotted line in Figure 4-13 (T-4 T-tail) should be below the red continuous line (T-2 T-tail) and the orange dotted line (T+1 T-tail) should be above. The difference in critical pressures between positive and negative yaw angles is however rather small and may be difficult to catch correctly by our numerical tools.

Finally, Figure 4-14 shows the evolution of the critical pressure with Mach number when a gap is added at the junction between the fuselage and the HTP. The presence of the gap spectacularly improves the predicted critical pressure for the T-2 T-tail. In addition, it would be very interesting to check if the same improvement would be seen for the T+1 and T-4 configurations.

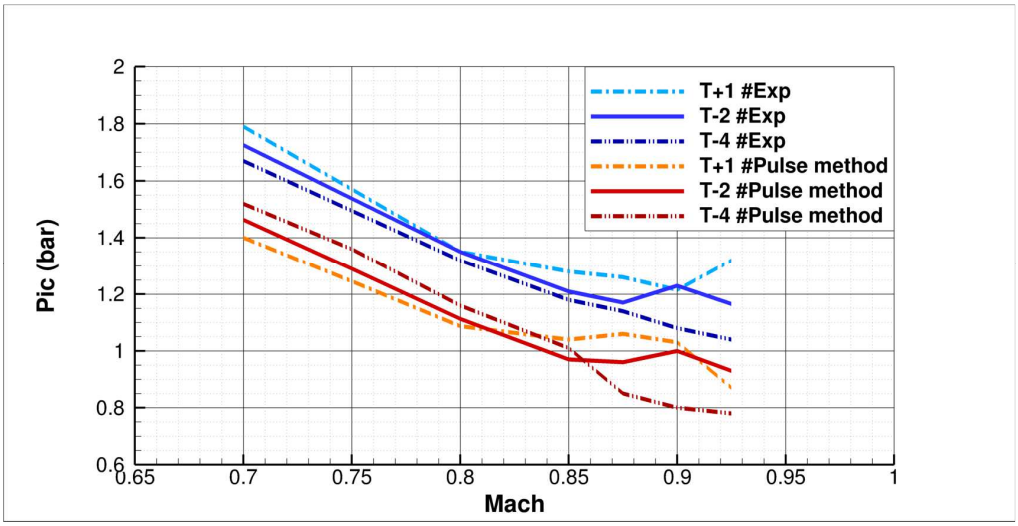

Figure 4-13: Comparison of the evolution of the critical stagnation pressure with Mach number between configurations T+1, T-2 and T-4 for verification of the yaw angle effect.

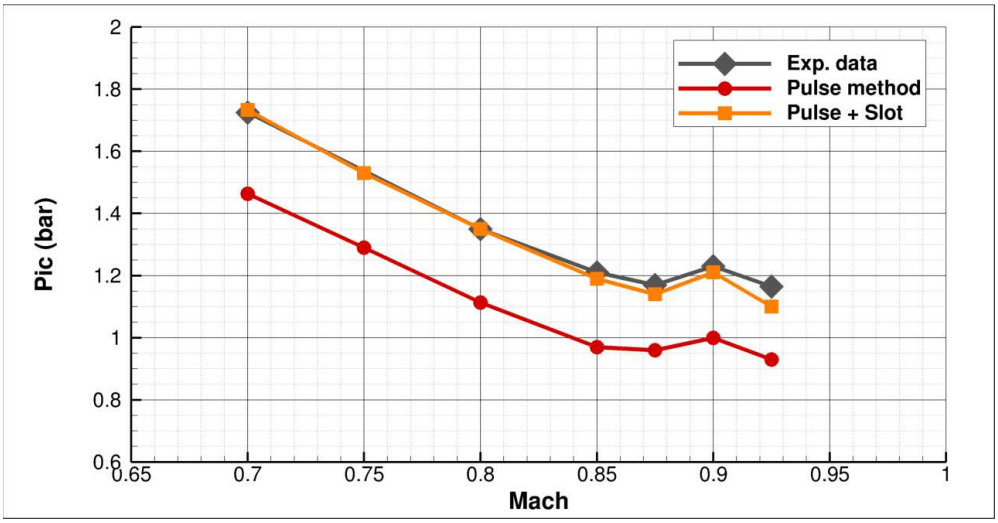

Figure 4-14: T-2 T-tail – Gap effect on the evolution of the critical stagnation pressure with Mach number

5 CONCLUSIONS

This paper presents the main results of the numerical restitution of the test campaign realized on a T-tail flutter model in subsonic and up to high transonic domains. Numerical results obtained with high-fidelity fluid-structure coupling methods such as the Pulse and the Direct Coupling methods were compared to Wind-Tunnel Test data and to results obtained with the low-fidelity DLM method.

Four configurations of T-tail were measured during the test campaign, but only three of them were considered in this paper and a particular attention is given to the effect of the yaw angle on the flutter phenomenon.

First, the paper focuses on the numerical restitution of the pressure measurements made during the new test campaign. Only a very small part of the numerical results has been presented but the

complete analysis of the results has shown that a very good correlation is obtained between the numerical and experimental steady pressure coefficients, even at higher Mach numbers. The steady pressure amplitude can even be locally improved by taking into account the 5 mm gap at the HTP/fuselage junction. The unsteady pressure coefficients were more difficult to predict, especially for their imaginary part, whose very small amplitude could only be predicted with a very fine time discretization. In the subsonic range, the correlation between the numerical and experimental unsteady coefficients was quite satisfactory. At higher Mach numbers, although most of the phenomena could be caught, the discrepancies between the numerical and experimental data increased. Again, the presence of the gap at the HTP/fuselage interface, allows an improved prediction of the unsteady pressure coefficients, at least for their real part.

Then, the numerical restitution of flutter measurements is presented in a second part of the paper. In this study, the flutter results were obtained with a modal basis issued from the Finite Element Model of Dassault-Aviation updated with GVT data. For the three T-tail geometries studied, the flutter predictions were disappointing because they showed a gap of about 0.25 bars between numerical and experimental data in terms of critical pressure. However, high-fidelity simulations performed with the Pulse method were capable to predict the good evolution of the critical pressure with Mach number, and to catch the Mach effect. In comparison, DLM was able to predict very precisely the critical pressure up to Mach numbers of 0.875. Therefore, this basic method, even if not capable to predict non-linear effects, remains an efficient tool in a first analysis process. In a last step, the addition of the 5mm gap at the HTP/fuselage junction results in a very good improvement of the predicted critical pressure of the T-2 T-tail. It would be very interesting to further verify this behavior on the T+1 and T-4 T-tail geometries.

ACKNOWLEDGMENTS

This work has been funded within the frame of the Joint Technology Initiative JTI Clean Sky 2, AIRFRAME Integrated Technology Demonstrator platform "AIRFRAME ITD" (contract N. CS2-GAM-AIR-2020-21-04) being part of the Horizon 2020 research and Innovation framework program of the European Commission.

REFERENCES

[1] Lanari V., Lepage A., Breus E., “T-tail transsonic flutter wind tunnel test – Part 1: Sealing system design and model testing”, *IFASD 2024*, Den Haag.

[2] Cambier L., Heib S., Plot S. (2013). The ONERA elsA CFD software : input from research and feedback from industry, *Mechanics & Industry***,** 14(3): 159-174.

[3] Van Zyl L., H., Mathews E., H. (2011). Aeroelastic analysis of T-tails using an enhanced Doublet Lattice Method, *Journal of Aircraft*, 48(3), 823-831.

[4] Geuzaine P., Brown G., Harris C., Farhat C. (2003). Aeroelastic dynamic analysis of a full F-16 configuration for various flight conditions, *AIAA Journal*, 41(3), 363-371.

[5] Nikbay K., Farhat C. (2001). Coupled analytical sensitivity analysis and optimization of three-dimensional nonlinear aeroelastic systems, *AIAA Journal*, 39(11), 2051-2061.

[6] Geeraert A., Lepage A., Stephani P., Feldmann D., Häberli W. (2017). Wind tunnel flutter tests of a U-tail configuration. Part 1: Model design and testing. International Forum on Aeroelasticity and Structural Dynamics, Como, Italy.

[7] Mamelle H., Broux G., Garrigues E. (2017). Wind tunnel flutter tests of a U-tail configuration. Part 2: Experimental and numerical results. International Forum on Aeroelasticity and Structural Dynamics, Como, Italy**.**

[8] Dat, R. and Meurzec, J-L. (1969). On the Flutter Calculations by the so-called "Reduced Frequency Scanning" Method, *La Recherche Aérospatiale*, 133, 41-44.

[9] Tran D.-M., Liauzun C., Labaste C. (2003). Method of Fluid-Structure Coupling in Frequency and Time Domains using Linearized Aerodynamics for Turbomachinery, *Journal of Fluids and Structures*, 17, 1161-1180.

[10] Albano E., Rodden W.P. (1969). A Doublet Lattice Method for Calculating Lift Distributions on Oscillating Surfaces in Subsonic Flows, *AIAA Journal*, 7(2), 279-285.

[11] Mortchelewiz G-D, Le Bihan D. (2018). Pulse method for aircraft flutter prediction, *58th IACAS*, Tel-Aviv, Israël.

[12] Dequand S., Geeraert A., Mortchelewicz G.-D. (2019). Innovative tail configuration: numerical vs wind-tunnel test data, *IFASD 2019*, Savannah, Georgia, USA.

COPYRIGHT STATEMENT